Feature Article:

Radar Doppler Frequency Measurements—Accuracy Versus SNR in Practical Processors

Nadav Levanon, **Department of Electrical Engineering, Systems Tel-Aviv University, Tel-Aviv, Israel**

INTRODUCTION

Doppler shift of a target-return provides the target's range-rate information. In the prevailing low-signal-to-noise ratio (SNR) scenes, the radar's coherent processing interval (CPI) determines the Doppler measurement resolution. Clutter joins thermal noise to render most scenes as low SNR. In low-SNR scenes, Doppler resolution defines also Doppler accuracy and the SNR value hardly enters the analysis. The Doppler assigned to a target detected in a specific range-Doppler cell is the cell's nominal Doppler value. Processing methods usually shape the Doppler response to minimize the mainlobe width and reduce sidelobes that can overlap neighboring Doppler cells.

Radar Doppler measurement will be demonstrated using a coherent train of pulses. The CPI will be long enough to contain many pulse repetition intervals (PRI). Furthermore, the Doppler frequency f_D of interest will be small enough to provide adequate number of samples (pulses) during one Doppler cycle, namely $f_D \, \mathrm{PRI} \ll 1$.

The three subplots in Figure 1 show received (noise free) Doppler-shifted coherent pulses after the intermediate frequency stage (top), the synchronously detected in-phase (*I*) samples (middle), and quadrature-phase (*Q*) (bottom subplot). The *n*th sample of the complex envelope is given by

$$u_n = I_n + jQ_n. \tag{1}$$

In a high-SNR scene, the phase of each received pulse can be measured, relative to the known phase of the transmitted pulse. The resulted phase ramp during one Doppler

Authors' current addresses: Nadav Levanon, Department of Electrical Engineering, Systems Tel-Aviv University, Tel-Aviv 6997801, Israel. (E-mail: levanon@tauex.tau.ac.il).

cycle (short CPI), or the Doppler cycle count (long CPI), can yield very accurate Doppler information. In that case, we will show that the standard deviation (STD) of the phase measurement error depends on the inverse of the square root of the SNR, as predicted by the Carmer-Rao [1], [2] lower bound.

In pulse-compression radar, each pulse is intrapulse phase coded or frequency modulated. The ensuing analysis will use pulses that are phase coded by a 13 element binary sequence (Barker 13). For simplicity, the receiver will not contain a mismatched filter, which is commonly used to reduce the range sidelobes.

PROCESSING LOW-SNR SCENE—THE "AMBIGUITY FUNCTION" APPROACH

Figure 2 describes a simple generic range-Doppler processor that can handle a low-SNR radar scene. Synchronous I&Q detection and sampling follow the IF amplifier. If the pulse is phase coded, then, the sampling period t_s is equal to or shorter than the code element duration t_b. T_r is the PRI. To obtain good Doppler resolution M identical pulses are processed coherently, yielding $\mathrm{CPI} = M \, T_r$. A matched filter precedes the Doppler processing. It is assumed that the intrapulse phase ramp, caused by Doppler shift, does not seriously degrade the sidelobe behavior of the delay response.

Doppler processing is handled by the interpulse Doppler compensation, known also as slow-time Doppler compensation. The present matched filter output joins the previous outputs from $M-1$ shift registers, each register produces delay equal to T_r, to create M inputs to an fast Fourier transform (FFT), all coming from the same delay (range cell). In some cases, a moving target indicator (MTI) precedes Doppler processing by the FFT. Its task is to attenuate very strong reflections from stationary near-clutter that can exceed the dynamic span of the following processing stages.

When the interpulse weight window is uniform, the M FFT outputs produce M cuts of the periodic ambiguity
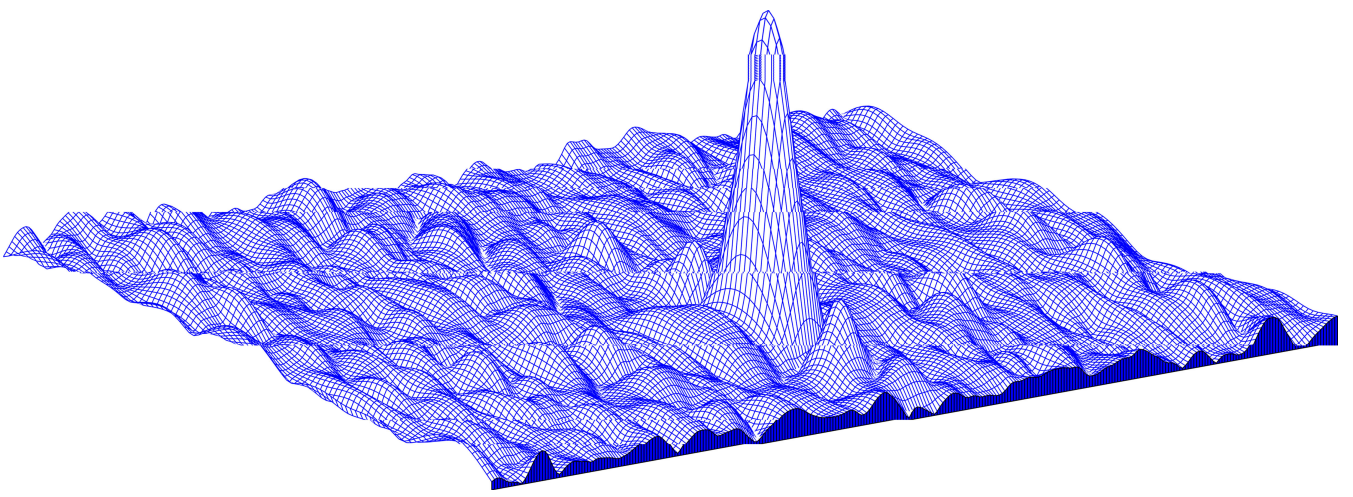
function (PAF) [3], [4]. This explains the name given to this approach. When the pulse duration t_p is short relative to the PRI, namely $t_p < T_r/2$ then the PAF is given by

$$\left| \chi_{MT_r} (\tau, \nu) \right| = \left| \chi (\tau, \nu) \right| \left| \frac{\sin(MT_r\pi\nu)}{M \sin(T_r\pi\nu)} \right| \qquad (2)$$

where $\chi(\tau, \nu)$ is the Woodward's ambiguity function [4] of a single pulse, τ is delay, and ν will represent Doppler shift (together with f_D). The Doppler resolution is given by the cut of (2) at zero delay. Setting $\tau = 0$ in (2) yields

$$\left| \chi_{MT_r} (0, \nu) \right| = \left| \chi (0, \nu) \right| \left| \frac{\sin(MT_r\pi\nu)}{M \sin(T_r\pi\nu)} \right|. \qquad (3)$$

One of the properties of the AF is that its zero-delay cut is independent of any phase or frequency modulation, but depends only on the magnitude of the pulse's complex envelope $u(t)$,

$$\left| \chi (0, \nu) \right| = \left| \int_{-t_p/2}^{t_p/2} |u(t)|^2 \exp(j2\pi\nu t) \, dt \right|. \qquad (4)$$

In our example the pulse is phase coded, but its amplitude is constant, which results in

$$\left| \chi(0, \nu) \right| = \left| \frac{\sin(t_p \pi \nu)}{t_p\pi \nu} \right|. \qquad (5)$$
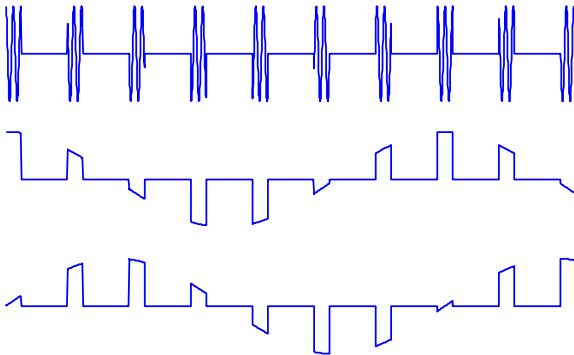

Figure 1.
Coherent I and Q sampling of a Doppler shifted pulse train.

Inserting (5) in (3) yields the expected Doppler response of a coherent train of M identical phase coded (or frequency modulated) pulses,

$$\left| \chi_{MT_r} (0, \nu) \right| = \left| \frac{\sin(t_p \pi \nu)}{t_p\pi \nu} \right| \left| \frac{\sin(MT_r\pi\nu)}{M\sin(T_r\pi\nu)} \right|. \qquad (6)$$

Using a decibel scale, Figure 3 displays (6), for the case of $M = 32$, $T_r/t_p = 5 \Rightarrow MT_r/t_p = 160$. For such a case, the first term on the right-hand side (r.h.s.) of (6) hardly influences the Doppler response. Its effect is seen by the attenuation of 0.6 dB of the recurrent lobes at $f \, MT_r = \pm 32$. Note that the Doppler resolution (defined as the separation between the mainlobe's peak and the first null) is $\Delta \nu = \Delta f = 1/(M \, T_r) = 1/\text{CPI}$.

Nonuniform weight windows, such as Hamming, Dolph-Chebyshev, [5], [6] can help reduce the sidelobes of the Doppler response, with a penalty of wider mainlobe. To avoid transmitting pulses of different amplitudes, the weight window appears only at the receiver side, causing mismatch, hence the SNR loss. Typical loss is about 1.5 dB (e.g., in the Hamming case). Figure 4 displays the normalized Doppler response when a Hamming window is used. Note the reduced Doppler sidelobes and the doubling of the Doppler resolution.

Figures 3 and 4 show that the Doppler resolution achieved by the processor outlined in Figure 2 is either $\Delta \nu = 1/(MT_r)$, without interpulse amplitude weight window, or $\Delta \nu = 2/(MT_r)$ when a Hamming weight window is used. To learn the two-dimensional range-Doppler response, we need to define a more specific waveform. To keep the example simple, we will add Barker 13 binary phase-coding to the previous example. With this choice, the duration of a code element is $t_b = t_p/13$. We will also add Doppler shift. Figure 5 displays the noise-free phase evolution along six (out of 32) received pulses. From a phase change during one PRI, $\Delta\phi = 0.5893$ rad, we can derive the normalized dimensionless Doppler shift $\nu t_b = 0.5893/(130\pi) = 0.0014$, $\nu T_r = 0.0938$, and finally $\nu MT_r = 3$. The last normalization is the one used in the delay-Doppler responses shown in Figures 6 and 7.
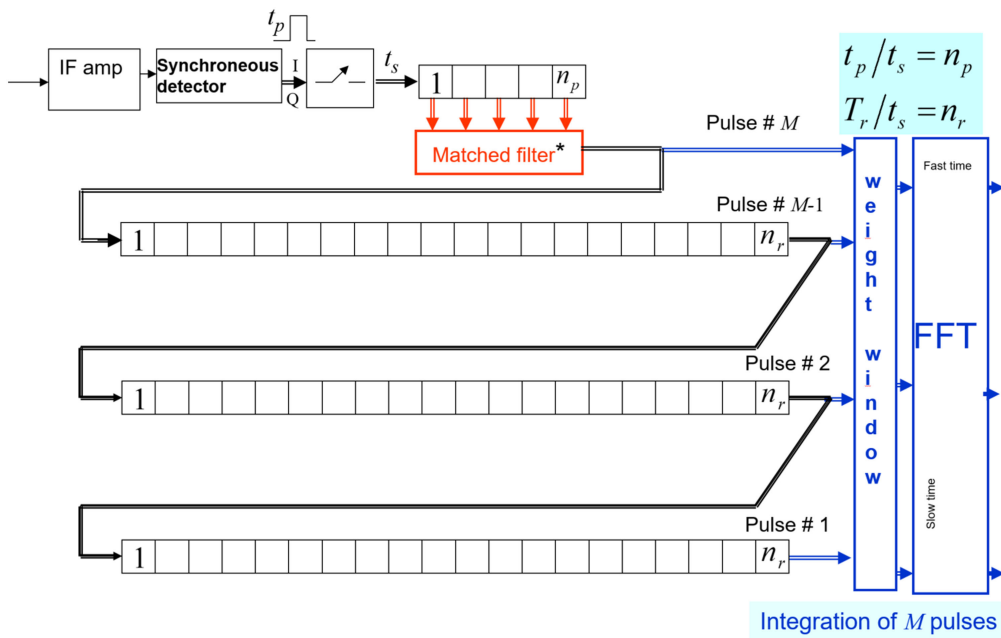
$$t_p/t_s = n_p$$
$$T_r/t_s = n_r$$

Figure 2.
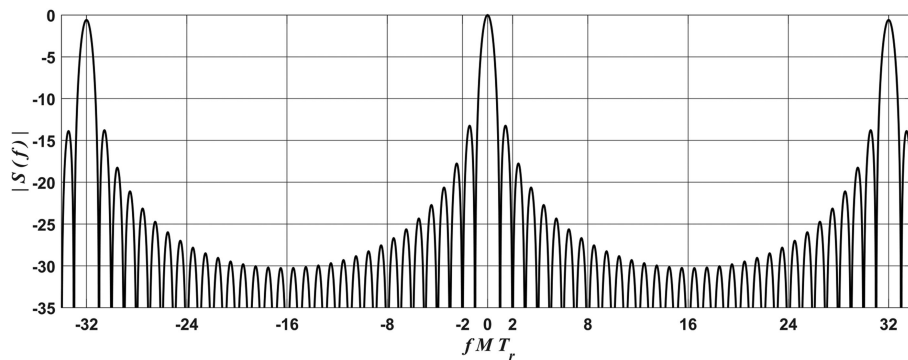Generic delay-Doppler processor of a coherent train of identical coded pulses.

Figure 3.
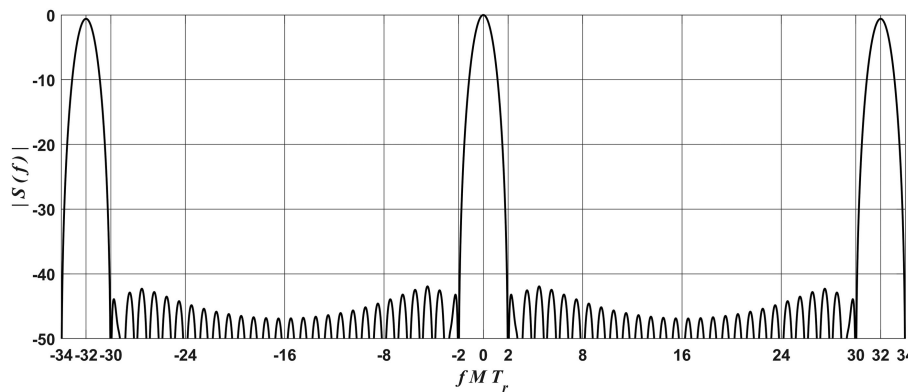Doppler response of an unweighted coherent train of 32 unimodular pulses.

Figure 4.
Normalized Doppler response of a coherent train of 32 pulses, Hamming amplitude weighted on receive.
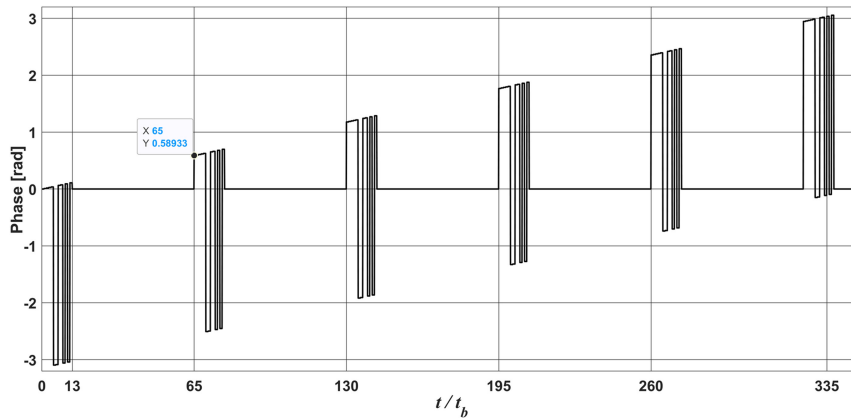
Figure 5.
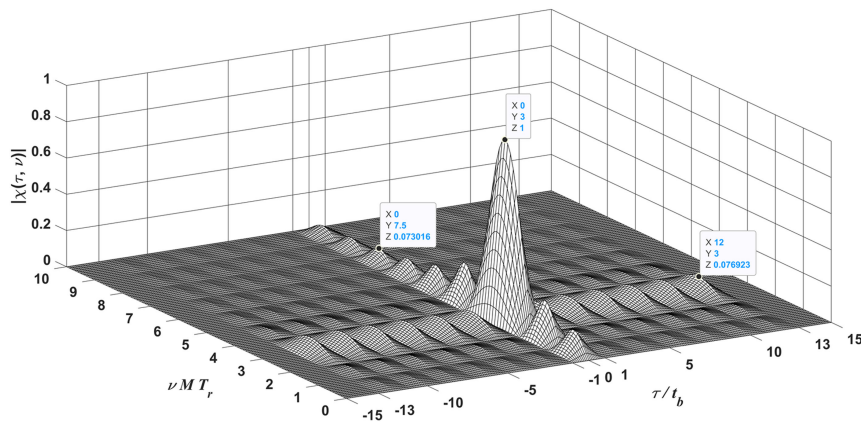Noise-free phase evolution of Doppler shifted 6 (out of 32) received pulses.

Figure 6.
Delay-Doppler response of the processor (uniform weight window) to the Doppler shifted waveform.
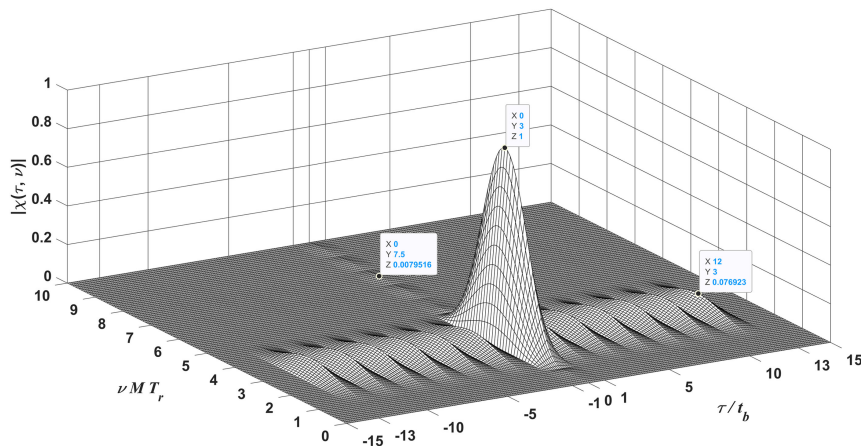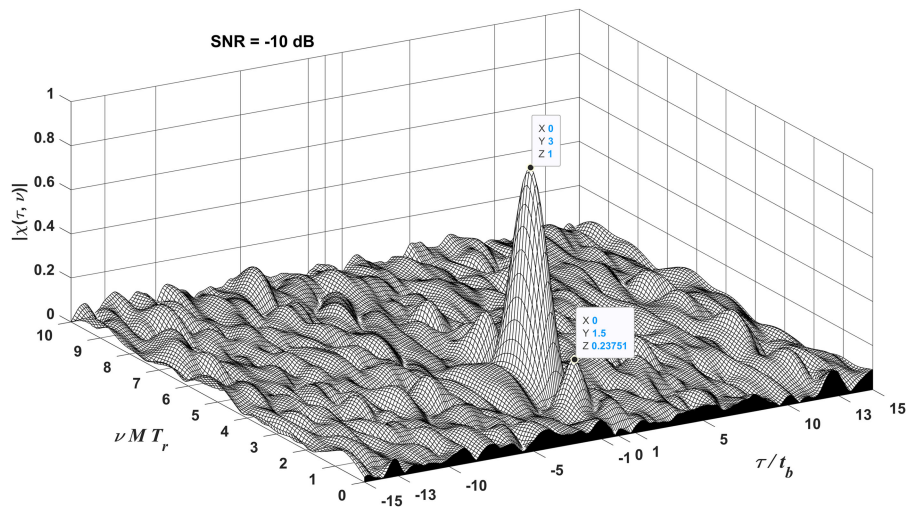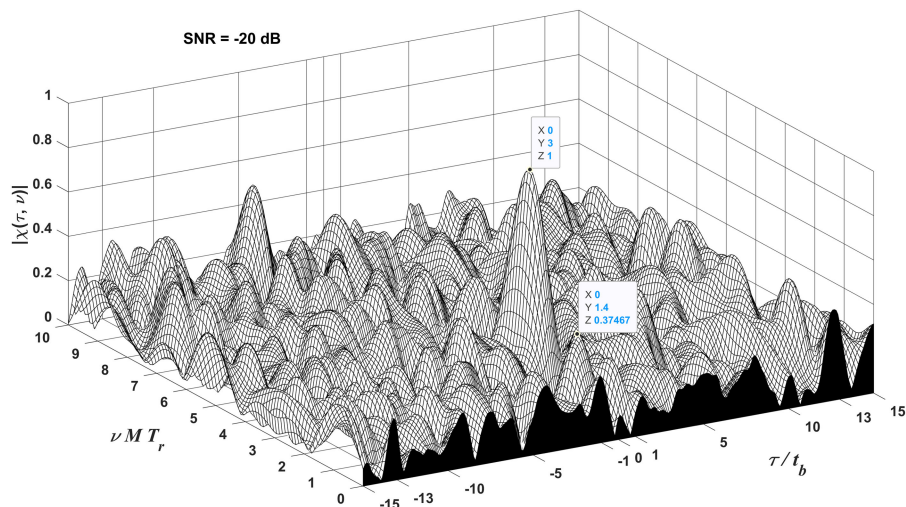

Figure 7.
Delay-Doppler response of the processor (Hamming weight window) to the Doppler shifted waveform.

Figure 6 presents the response when a uniform weight window is used. As expected, the mainlobe is located at $\tau = 0$, $\nu MT_r = 3$. The range sidelobes are the well-known Barker 13 sidelobes with peak sidelobe level (PSL) of $1/13 = 0.0769$. The Doppler sidelobes match Figure 3. Figure 7 presents the response when a Hamming weight window is used. The Doppler main-lobe width doubled and the Doppler sidelobes dropped to typical peaks of $20\log_{10}(0.007952) = -42$ dB. While the matched filter did not compensate the Doppler-induced intrapulse phase ramp, we see no effect on the range sidelobes pattern and heights. In case of a longer

Figure 8.
Normalized delay-Doppler response to the Doppler shifted waveform, SNR = −10 dB, $M = 32$.

Figure 9.
Normalized delay-Doppler response to the Doppler shifted waveform, SNR = −20 dB, $M = 32$.

code and higher duty cycle, some degradation should be expected.

Note that Figure 7 displays the normalized response, in which the peak attains a unit value. Without normalization, a loss due to a Hamming window on receive would have caused a drop of about 1.5 dB in the peak.

With this kind of Doppler processing, the duration of the CPI determines the Doppler resolution. The first Doppler null, next the peak at $\nu = 0$, will appear at $\nu = 1/\text{CPI}$. Using a nonuniform interpulse weight window (e.g., Hamming) will approximately double the Doppler resolution. A target detected by threshold crossing, at a specific output of the FFT (in the unavoidable presence of noise and clutter), is assigned the Doppler shift value associated with that FFT output. Low SNR does not alter the resolution, but can prevent threshold crossing, causing missed detection. Figures 8 and 9 show the delay-Doppler responses of the signal used so far, at SNR values of −10 dB and −20 dB, respectively.

We should point out that in the processor producing Figures 8 and 9, the complex envelope of the signal-plus-noise passed through a low-pass Butterworth filter of order one and $\omega_n = 0.15$; and there were ten samples per code element. Uniform weight window was used; hence, the noise-free response to compare is the one in Figure 6. The response in Figure 8 indicates reasonable probability of detection, while lowering the threshold below the peak value in Figure 9 is likely to cause high probability of false alarm. Note that the stated SNR is per sample and before the filter.

The "Ambiguity Function" Doppler frequency estimation approach, discussed in this section, aims at the prevailing low-SNR radar scene. However, in high-SNR scenes, it can be modified to produce the frequency
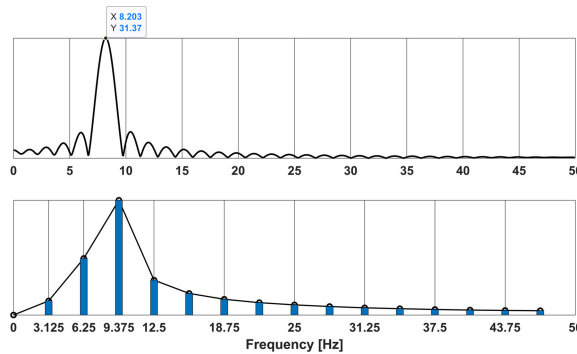
Figure 10.
(Top) True spectrum, after LPF, of an 8.2-Hz single tone; (Bottom) FFT outputs of 16 samples. Noise free case.
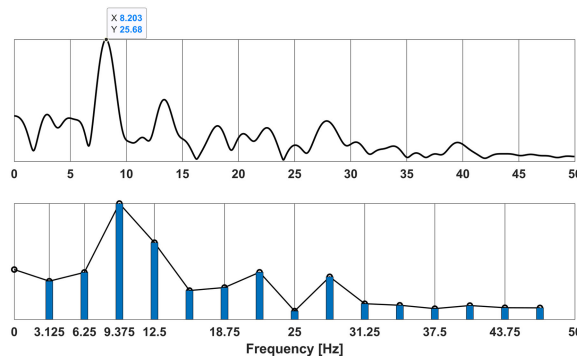

Figure 11.
(Top) Spectrum after LPF, of a noisy 8.2-Hz single tone; (Bottom) FFT outputs of the 16 samples. SNR = –2 dB per sample.

estimation with better accuracy than the resolution $\Delta v = \Delta f = 1/(MT_r) = 1/\text{CPI}$. In a high-SNR scene, zero-padding the FFT can be used. Furthermore, if the exact Doppler frequency is located between two nominal frequencies, corresponding to two neighboring FFT outputs, the estimated frequency need not be the nominal frequency of the FFT cell whose output is the highest. Interpolation can be used to estimate a more exact location of the spectrum peak. A qualitative example is demonstrated in Figures 10 (noise-free) and 11 (SNR = –2 dB, per sample).

In the noise-free case (see Figure 10), interpolating the lower subplot would have correctly placed the spectral peak to the left of the 9.375 Hz cell. In the low-SNR case (see Figure 11), interpolation would have erroneously placed the peak at about half way between 9.375 and the 12.5 Hz cells.

PROCESSING HIGH-SNR SCENES

In rare radar scenes, where the signal-to-clutter plus noise ratios are high, the concept of Doppler measurement accuracy (or precision) becomes relevant, including its dependence on SNR. By accuracy, we refer to the noise-induced error standard deviation. Mean error, usually caused by other error sources, will be ignored [7].

Returning to the Doppler shifted, noise-free, phase evolution in Figure 5, our ad-hoc Doppler measuring concept will be based on measuring the phase of each pulse (after compression). Assuming no change of the target's range rate during the CPI, the Doppler frequency will be derived from the slope of the unwrapped line connecting the measured phases.

PHASE MEASUREMENT

The phase of a single compressed pulse will be determined by $\tan^{-1}(Q_p/I_p)$, where Q_p, I_P are the quadrature and in-phase values of the sample corresponding to the peak of the matched filter response (i.e., the correlation of the received coded pulse and the noise-free coded reference). In high-SNR scenes finding the closest sample to the peak is rather simple if there are enough samples per code elements.

Figure 12 (top) shows the complex envelope of the Barker 13 signal used in the phase measurement example. *xs* is the pre LPF waveform and *ys* is the post LPF waveform. Note that the complex envelope is real, having no
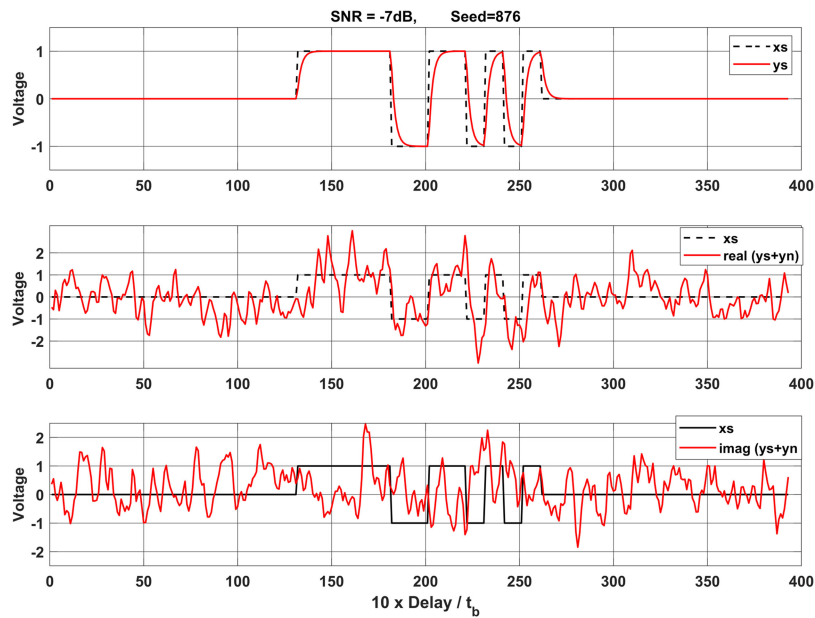
Figure 12.
Noise-free waveform before and after LPF (top). The real part of the received signal + noise (middle) and the imaginary part (bottom). SNR = −7dB.
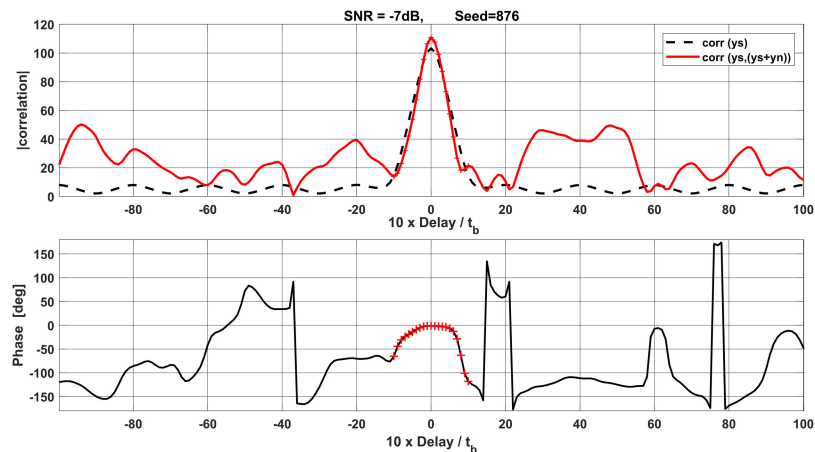

Figure 13.
Magnitude (top) and phase (bottom) of the cross-correlation output.

imaginary component. This fact implies that the reference signal's phase is zero. The red solid lines in the middle and bottom subplots show the real and imaginary values after complex random noise is added to the low-pass filtered Barker 13. This is a low-SNR case, in which SNR = −7dB. Note that there are ten samples per coding bit duration t_b. Note also that the stated SNR is per sample and before the filter.

The receiving processor performs cross correlation between the noise-free reference signal *ys* and the noisy signal *ys+yn*. Figure 13 displays the magnitude (top) and phase (bottom) of the cross correlation. The display zooms on ten coding bits, namely, the delay span is $-10 \leq \tau/t_b \leq 10$. At this SNR level, the correlation

magnitude peak is still well defined above the sidelobes, allowing simple determination of the target's delay. One possible technique is to use convolution with a split-gate [8], and to find the zero-crossing point of the convolution output. A simpler technique is to choose the mid delay sample between two threshold crossings: at the rise and fall of the convolution mainlobe. The phase value (bottom plot) shows the expected zero phase value around the delays corresponding to the peak of the correlation's magnitude.

Monte Carlo simulation, repeated 5000 times at each SNR value, produced the phase measurement error STD as function of SNR as presented in Figure 14. A line (dash, red) representing $\phi_{\mathrm{STD}} = 2.095/\sqrt{\mathrm{SNR}}$ was fitted
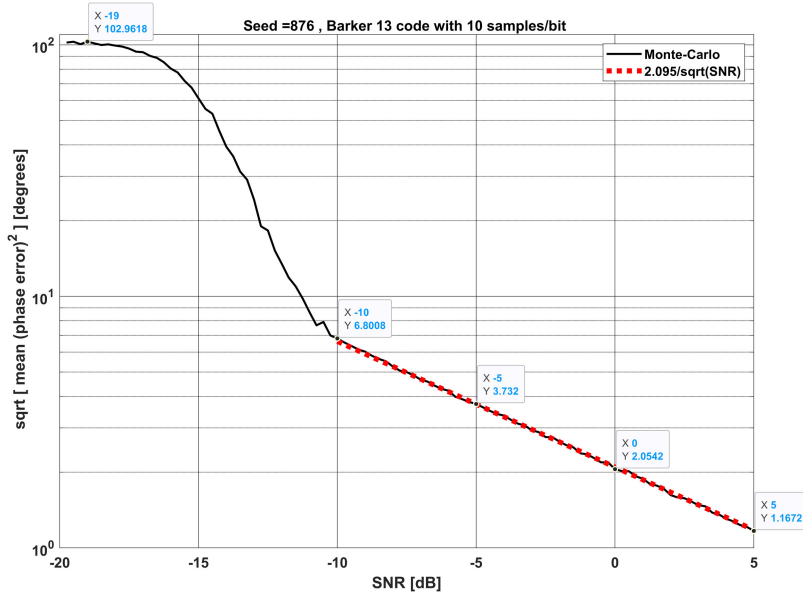
Figure 14.
Phase error STD as function of SNR, obtained from Monte Carlo simulation.

to the $-10 \leq \mathrm{SNR} \leq 5$ dB span of the curve to demonstrate the expected error dependence on $\mathrm{SNR}^{-1/2}$.

The phase error curve demonstrates the three typical zones of error versus SNR. In the *high-SNR* zone (on the right), the phase error follows a $\mathrm{SNR}^{-1/2}$ law. In the left zone, at very low SNRs, the error curve is flat around $\sqrt{\mathrm{var}(\phi)} \approx 103°$, as seen in the left-most data tip. It is known as the *no information* zone and the error level as the *a priori bound*. When the SNR is very low, the measured phase is uniformly distributed over all possible phase values, yielding

$$
\begin{aligned}
\mathrm{var}(\phi) &= \frac{1}{360} \int_{-180}^{180} \phi^2 \mathrm{d}\phi \\
&= \frac{1}{180} \int_{0}^{180} \phi^2 \mathrm{d}\phi = \frac{1}{180} \left[\frac{\phi^3}{3} \right]_{0}^{180} \\
&= \frac{180^2}{3} \Rightarrow \sqrt{\mathrm{var}(\phi)} = \frac{180}{\sqrt{3}} = 103.9°.
\end{aligned}
\tag{7}
$$

The two SNR zones are connected by the *transition* zone, in which the phase error increases rapidly as the SNR drops. Using a longer coding sequence will allow accurate measurements at lower SNR values. With a 48 element Minimum Peak Side Lobe code, the high-SNR zone of the curve will shift left by $10\log_{10}(48/13) = 5.67$ dB.

FROM PHASE MEASUREMENT TO FREQUENCY MEASUREMENT

Frequency cannot be measured instantly. Accurate estimate of the Doppler frequency can be derived from the set of measurements of the phase of each received pulse in the coherent train (e.g., the 32 pulses used in the section "Processing Low SNR Scene—The "Ambiguity Function" Approach). The known PRI of the transmitted pulses can ease finding the expected location of the correlation peak, from where the phase value of each pulse is extracted.

The assumption that the target's range rate does not change during the CPI implies that the noise-free phase measurement should be a linear function of time. The slope of the line is the angular frequency ω of the Doppler shift,

$$
\phi(t_m) = \phi_0 + \omega t_m + \upsilon_m, \quad t_m = mT_r, \\
m = 0, 1, \ldots, M-1
\tag{8}
$$

where T_r is the PRI and υ_m is the error of the measured phase of the mth pulse.

We will also assume that the phase measurements errors are uncorrelated and have identical variance σ_ϕ^2 so that the phase errors covariance matrix is

$$
R_\phi = \sigma_\phi^2 I
\tag{9}
$$

where I is an identity matrix of size M. We will use linear least square (LS) to estimate the two line parameters, defined by the *parameters* vector

$$
\mathbf{x} = \begin{bmatrix} \phi_0 & \omega \end{bmatrix}^T
\tag{10}
$$

from the M phase measurements, defined by the *measurements* vector

$$
\phi = \begin{bmatrix} \phi_1 & \phi_1 \ldots \phi_m \ldots \phi_M \end{bmatrix}^T.
\tag{11}
$$

Table 1.

Normalized Frequency error STD versus SNR				
SNR [dB]	−7	−5	0	5
$\sigma_\phi\,°$	$5°$	$4°$	$2°$	$1.2°$
$MT_r\sigma_{f,}\,(M=32)$	$1/20=0.05$	$1/25=0.04$	$1/51=0.0196$	$1/85=0.0118$

We will also arrange the phase measurements errors in an *errors* vector

$$\boldsymbol{\upsilon} = [\,\upsilon_1 \quad \upsilon_1 \ldots \upsilon_m \ldots \upsilon_M\,]^T. \tag{12}$$

Finally, we define the (M x 2) matrix **H** that will allow us to describe the M equations in (8) as the M-dimensional *measurements* vector in (11)

$$\mathbf{H} = \begin{bmatrix} 1 & 1 & 1 & \ldots & 1 & \ldots & 1 \\ 0 & T_r & 2T_r & \ldots & mT_r & \ldots & (M-1)T_r \end{bmatrix}^T. \tag{13}$$

The resulted matrix equation is

$$\phi = \mathbf{Hx} + \boldsymbol{\upsilon}. \tag{14}$$

The well-known [9] LS solution of the *parameters* vector is

$$\hat{\mathbf{x}}_{\text{LS}} = \left(\mathbf{H}^T\mathbf{H}\right)^{-1}\mathbf{H}^T\phi. \tag{15}$$

Well known also is the covariance of the errors of the estimated parameters

$$\mathbf{P} = E\big[\hat{\mathbf{x}}_{\text{LS}}\hat{\mathbf{x}}_{LS}^T\big] = \sigma_\phi^2\left(\mathbf{H}^T\mathbf{H}\right)^{-1}. \tag{16}$$

Inserting (13) in (16) yields

$$\mathbf{P} = \sigma_\phi^2\left(\mathbf{H}^T\mathbf{H}\right)^{-1} = \sigma_\phi^2 \frac{12}{M^4 - M^2} \begin{bmatrix} \frac{1}{6}M(M-1)(2M-1) & \frac{-1}{2}M(M-1)/T_r \\ \frac{-1}{2}M(M-1)/T_r & M/T_r^2 \end{bmatrix}. \tag{17}$$

The error variance of the angular Doppler frequency $\boldsymbol{\omega}$ is $\mathbf{P}_{2,2}$, hence

$$\sigma_\omega^2 = \frac{12}{(MT_r)^2(M - 1/M)}\sigma_\phi^2. \tag{18}$$

We will convert (18) to Doppler frequency $f = \omega/(2\pi)$, perform square root and normalize the frequency to create a dimensionless variable by multiplying the frequency by the CPI, i.e., by MT_r,

$$MT_r\sigma_f = \frac{\sigma_\phi}{\pi}\sqrt{\frac{3}{M - 1/M}}. \tag{19}$$

The important expression in (19) says that the SNR dependence of the normalized frequency error $MT_r\sigma_f$ is shaped like the SNR dependence of the phase error, multiplied by an expression that is a function of M. Using the data from Figure 14, we can construct a short table expressing that dependence.

The two top rows of Table 1 were taken from Figure 14. From the phase error STD (middle row), the dimensionless normalized *frequency error* STD (bottom row) is calculated using (19). Recall that the normalized *frequency resolution* of the conventional FFT processor, at all SNR values, is $MT_r\Delta f = 1$. Therefore, the values at the bottom row indicate the ratio σ_f/Δ_f by which the *frequency error*, obtained through phase measurement of each pulse in the CPI, is smaller than the *frequency resolution* obtain through the FFT processing of a pulse train. The bottom row therefore says that over the span $-7 \leq \text{SNR} \leq 5$ dB, the above approach of measuring Doppler frequency shift is better than the "ambiguity function" approach by factors of 20 to 85, respectively.

FIELD TRIAL IN A HIGH-SNR SCENE

In order to create a high-SNR scene, signal transmitted by a stationary radar was recorded by a receiver on board an airborne target. The flight direction was slightly off cross range and the radial distance was about 6 km. The transmitted signal was a coherent train of binary-coded pulses using a 48 element code, with PRF = 1300 s^{-1} and $t_p = 96$ μs. The receiver's oscillator was, of course, different from the transmitter's oscillator and a small constant frequency difference was added to the Doppler frequency. Phase unwrapping and outliers' removal were involved in the processing of the phase measurement. Figure 15 displays the recorded unwrapped phase of the airborne received pulses along a flight section of 15 s. Four linear sections are marked, from which Doppler (+ oscillator bias) frequencies could be calculated accurately. The accumulated phase of 5000 radians corresponds to a Doppler cycle count of 800 cycles. At the signal's wavelength of 0.5769 m, this accumulation indicates a range change of 461 m. Therefore, during those 15 s, the average range rate was about 30 m/s.

A brief historical note: The concept of Doppler count is associated with the TRANSIT navigation satellite system
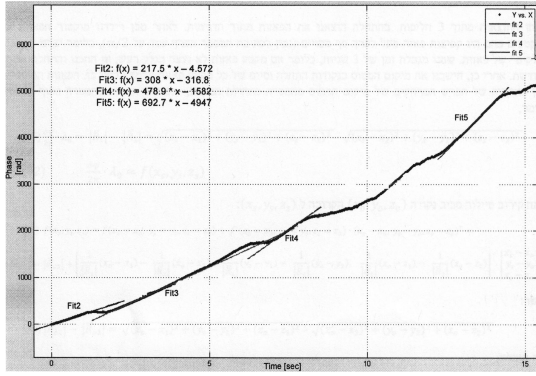
Figure 15.
Recorded phases of about 20000 coherent radar pulses received by an airborne receiver.

[10]. The concept and its implementation in TRANSIT navigation receivers are clearly described in [11].

PULSE-PAIR DOPPLER PROCESSING

Another high-SNR approach finds application in weather radars [12, 7(Ch. 5)]. A rain cloud usually occupies more than one spatial cell and a given cell contains an extended target with a relatively wide Doppler spectral width. The parameters of interest are reflection intensity, average Doppler frequency, and the Doppler spectral width. We will consider only the average Doppler frequency, which is easily obtained from the first leg of the Doppler signal's autocorrelation [12].

Doppler signal synchronously detected from a single moving scatterer will be a single-tone sinewave at a frequency f_D, sampled at a rate equal to the radar PRF. Within the duration of CPI $= MT_r$, the sampled sinewave is given by

$$y[m] = Ae^{j2\pi f_D mT_r}, \quad m = 0, \ldots, M-1. \tag{20}$$

The first coefficient of the signal's autocorrelation is given by

$$R_y[1] \equiv \sum_{m=0}^{M-2} y[m]y^*[m+1]. \tag{21}$$

Using (20) in (21) yields

$$R_y[1] = \sum_{m=0}^{M-2} Ae^{j2\pi f_D mT_r} A^* e^{-j2\pi f_D(m+1)T_r}$$
$$= |A|^2 \sum_{m=0}^{M-2} e^{-j2\pi f_D T_r} = |A|^2 e^{-j2\pi f_D T_r} \sum_{m=0}^{M-2} (1) \tag{22}$$
$$\therefore R_y[1] = |A|^2 (M-1)e^{-j2\pi f_D T_r}.$$

The Doppler frequency appears in the argument of the first leg of the signal's autocorrelation

$$\arg\{R_y[1]\} = -2\pi f_D T_r. \tag{23}$$

Hence, the estimated Doppler frequency is given by

$$\hat{f}_D = \frac{-1}{2\pi T_r} \arg\{R_y[1]\}. \tag{24}$$

An example of pulse-pair processing is demonstrated by a real signal constructed from two close sinewaves of equal amplitude and carriers at $f_1 = 7.6$ Hz and $f_2 = 8.2$ Hz. The detailed expression is

$$s(t) = \text{Re}\{\exp(j2\pi f_1 t) + \exp[j(2\pi f_2 t - 4\pi/7)]\}. \tag{25}$$

The signal and its power spectrum are shown in Figure 16.

In a noise-free case and two sinewaves of the same amplitude, the estimated Doppler frequency was exactly at the middle frequency 7.9 Hz. In the presence of noise, the random frequency error will be a function of the SNR and the number M of pulses within the CPI. As can be deduced from (21), the lower limit is $M = 2$ pulses. This
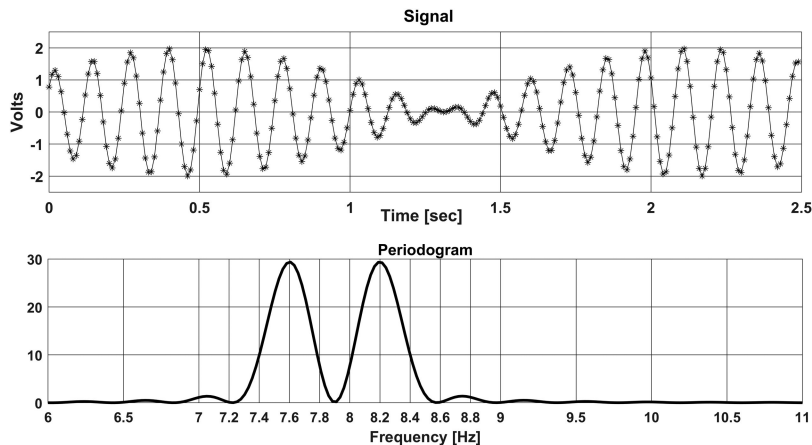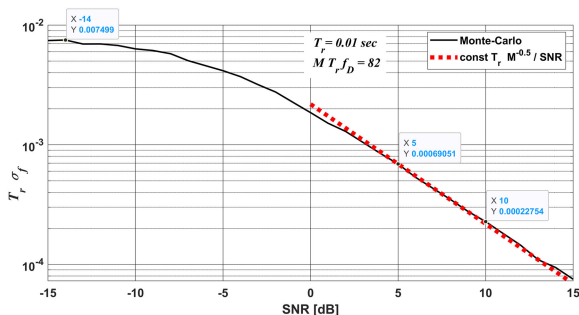

Figure 16.
Two sinewave signals (top) and their spectrum (bottom).

Figure 17.
Frequency error STD versus SNR, using the pulse-pair approach, $MT_r = 10$ s, $M = 1000$.

explains the name "pulse-pair." The "pulse-pair" approach can be used also to measure the Doppler shift of a radar return from a small target, rather than a rain cloud. In that case, the detected Doppler signal is a noisy sine wave. The dependence on *SNR* of the frequency measurement error of *M* samples of a single frequency sinewave, using the "pulse-pair" approach, is described next.

Monte Carlo simulations (see Figure 17) were performed for estimating the frequency of a single sinewave at 8.2 Hz with a noise span of $-15 \text{ dB} \leq \text{SNR} \leq 15 \text{ dB}$. The simulations reveal that the frequency error STD, obtained by the "pulse-pair" method at high *SNR*, is proportional to the inverse of the *SNR*, rather than to the inverse of $\sqrt{\text{SNR}}$, as was the case in the section "From Phase Measurement to Frequency Measurement." The other parameters of the simulation were $T_r = 0.01$ s and $M = 1000$, yielding $\text{CPI} = MT_r = 10$ s. At a Doppler frequency of 8.2 Hz, the CPI contained 82 cycles. The Monte Carlo simulations reveal dependence of the error of the measured normalized frequency $T_r \sigma_f$ on both SNR and the number *M* of samples (= pulses) within the CPI, according to the expression

$$T_r \sigma\left(\hat{f}_D\right) \quad \alpha \quad T_r M^{-1/2}/\text{SNR}. \tag{26}$$

The dependence of error STD on SNR^{-1} (rather than on SNR$^{-1/2}$) is revealed by the identical slope of the dotted red line and the simulation result. The dependence on $M^{1/2}$ is learned from the fact that the dotted red line will remain aligned with the Monte Carlo result despite changes in the parameter *M*. The error dependence on SNR^{-1} can be seen also in (2.11) in [12], when setting the spectrum width (w) to zero. The additional dependence on *M* is also in agreement with [12]. In Figure 17, *a priori bound* in the *no-information* SNR zone states what is the STD of the frequency measurement when there is no signal, just random noise. It is therefore determined mostly by the frequency response of the filter used. In Figure 17 the high-SNR zone begins at about SNR = 2 dB, where the normalized error is

$$T_r \sigma_f = 0.0013 \Rightarrow \sigma_f \bigg|_{T_r=0.01} = 0.13 \text{ Hz}. \tag{27}$$

Namely, at an SNR = 2 dB and CPI = 10 s, the nominal frequency of 8.2 Hz is measured with an error STD of 0.13 Hz. Example of the signal + noise, with SNR (before LPF) of 2 dB is shown in Figure 18. The plot contains 2 s out of a CPI of 10 s.

CONCLUSION

The accuracy of frequency measurement in radar and its dependence on SNR was demonstrated using three approaches: (a) The classical Pulse-Doppler processor that performs FFT on the same-delay returns from *M* consecutive pulses. We labeled it as the "ambiguity function" approach. (b) The "Doppler count" approach, in which the phase of each returning pulse is measured and the Doppler frequency is estimated from the slope of the phase ramp,
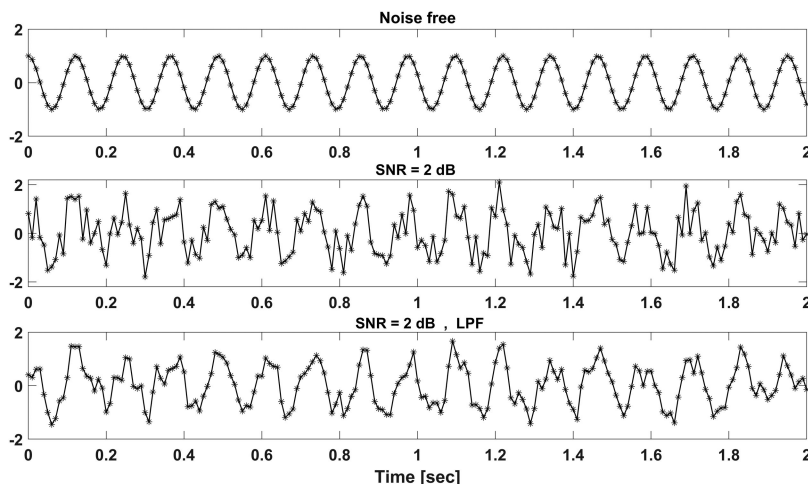
Figure 18.
2 s of 8.2-Hz sinewave: noise-free (top), SNR = 2 dB (middle), after LPF (bottom).

after unwrapping. (c) The "pulse-pair" approach, developed for early weather radars, in which the center frequency of the Doppler shift spectrum is calculated from the first leg of the signal's autocorrelation. The error attained in approach (a) is SNR independent, down to an SNR level below which detection fails. At high-SNR scenes, approach (b) demonstrates error STD dependence on $SNR^{-1/2}$, which is a classical estimation behavior at high SNR. In approach (c), our simulations confirm and demonstrate a frequency error STD dependence on SNR^{-1}, which is rather poor compared to approach (b), but simpler to implement.

REFERENCES

[1] C. E. Cook and M. Bernfeld, *Radar Signals an Introduction to Theory and Applications*. New York, NY, USA: Academic, 1967, ch. 5.

[2] H. L. Van Tress, *Detection, Estimation, and Modulation Theory, Part III*. New York, NY, USA: Wiley, 1971, sec. 10.2.

[3] N. Levanon and E. Mozeson, *Radar Signals*. New York, NY, USA: Wiley, 2004, sec.3.6.

[4] N. Levanon, "The periodic ambiguity function—Its validity and value," in *Proc. IEEE Int. Radar Conf.*, Washington, DC, USA, 2010, pp. 204–208.

[5] F. J. Harris, "On the use of windows for harmonic analysis with the discrete Fourier transform," *Proc. IEEE*, vol. 69, no. 1, pp. 51–83, Jan. 1978.

[6] K. M. M. Prabhu, *Window Functions and Their Applications in Signal Processing*. Boca Raton, FL, USA: CRC Press, 2018.

[7] M. A. Richards, *Fundamentals of Radar Signal Processing*, 2nd ed. New York, NY, USA: McGraw-Hill, 2014, ch. 7.

[8] D. K. Barton and H. R. Ward, *Handbook of Radar Measurement*. Dedham, MA, USA: Artech House, sec. 3.5.

[9] H. W. Sorenson, *Parameter Estimation: Principles and Problems*. New York, NY, USA: Marcel Dekker, 1980.

[10] W. H. Guier and G. C Weiffenbach, "A satellite Doppler navigation system," *Proc. IRE*, vol. 48, no. 4, pp. 507–516, Apr. 1960.

[11] T. A. Stansell, "The TRANSIT navigation satellite system," Magnavox Rep. R-5933A, Jun. 1983. [Online]. Available https://www.ion.org/museum/files/TransitBooklet.pdf Accessed on: Jul. 24, 2019.

[12] F. C. Brenham, H. L. Groginsky, A. S. Soltes, and G. A Works, "Pulse pair estimation of Doppler spectrum parameters," Raytheon Rep., AFCRL-72-0222, Mar. 30, 1972. [Online]. Available: https://apps.dtic.mil/dtic/tr/fulltext/u2/744094.pdf, Accessed on: Jul. 24, 2019.